Cement and Concrete Composites 121 (2021) 104039

Contents lists available at ScienceDirect

Cement and Concrete Composites

journal homepage: http://www.elsevier.com/locate/cemconcomp

3D concrete printing of permanent formwork for concrete column construction

Binrong Zhu [a], Behzad Nematollahi [b], Jinlong Pan [a,c,*], Yang Zhang [a], Zhenxin Zhou [a], Yamei Zhang [c,d]

[a] Key Laboratory of Concrete and Prestressed Concrete Structures of Ministry of Education, School of Civil Engineering, Southeast University, Nanjing, 211189, China
[b] Center for Smart Infrastructure and Digital Construction, Swinburne University of Technology, 3122, Hawthorn, Australia
[c] Nanjing Institute for Intelligent Additive Manufacturing Co. Ltd, Nanjing, 211800, China
[d] Jiangsu Key Laboratory of Construction Materials, Southeast University, Nanjing, 211189, China

ARTICLE INFO

Keywords:
Rheological properties
Structural build-up
Permanent formwork
3D concrete printing
Concrete column

ABSTRACT

This study investigated 3D concrete printing of permanent formwork for concrete column construction. The effect of different hydroxypropyl methyl cellulose (HPMC) contents (0, 0.0003 and 0.0006 by mass of binder) and the water-to-binder (W/B) ratios (0.27, 0.29 and 0.31) on the rheological properties, structural build-up and mechanical performance were studied using several mixtures for manufacture of the permanent formworks. The results showed that the mixture with the HPMC = 0.0006 and the W/B = 0.27 showed the maximum static yield stress, largest thixotropy and maximum green strength, and thereby selected as the optimum mixture. The plastic failure of the optimum mixture was also predicted using a thixotropy model and was compared with the experimental results. Subsequently, three concrete columns with different longitudinal steel reinforcement ratios (0.0%, 1.9% and 2.5%) were constructed using the printed concrete as the permanent formwork and tested in compression. Good bonding was observed at the interface of the cast-in-place concrete and the printed concrete permanent formwork. In addition, it was observed that the initial stiffness, the maximum bearing capacity and the corresponding longitudinal displacement of the concrete columns increased, as the longitudinal reinforcement ratio increased. The counterpart concrete columns using the conventional formworks were also constructed and tested for comparison. In comparison, the concrete columns made using the printed concrete as the permanent formwork obtained a higher stiffness and bearing capacity than the counterpart conventional concrete columns. The reasons for the differences are explained.

1. Introduction

3D concrete printing (3DCP) is a rapidly emerging construction process combining materials technology and digital technologies to build 'free-form' concrete structures layer-by-layer without the use of formwork. 3DCP can potentially provide high quality and a wide range of construction geometries with less construction time, cost and wastages due to the removal of the formwork [1,2]. The formwork represents 35%–60% of the overall costs of concrete construction [3]. In addition, the formwork forms a major part of the construction waste, as it is typically made of timber and all of it is discarded sooner or later [2,4].

In recent years, few emerging 3DCP technologies such as Contour Crafting, Concrete Printing, D-shape and Digital Fabrication have been developed. However, the application of 3DCP in industry is still in its primary stage, and further in-depth research is needed to overcome challenges to be able to fully utilize this technology in construction industry. One of the main challenges is that conventional steel reinforcement is hard to be included in the 3DCP process. Several research studies have been conducted to tackle this challenge. For example, researchers explored the possibility of using micro cables embedded inside the printed layers as reinforcement in 3D printed concrete [5,6]. In addition, the possibility of using different short fibers as a partial/complete replacement of steel rebars in 3D printed concrete have been investigated in several studies [7–11].

Another possible solution to tackle the reinforcement challenge is to use 3DCP technology to print a permanent (stay-in-place) concrete

* Corresponding author. Key Laboratory of Concrete and Prestressed Concrete Structures of Ministry of Education, School of Civil Engineering, Southeast University, Nanjing, 211189, China.
E-mail address: cejlpan@seu.edu.cn (J. Pan).

https://doi.org/10.1016/j.cemconcomp.2021.104039
Received 9 October 2020; Received in revised form 23 February 2021; Accepted 29 March 2021
Available online 15 April 2021

Table 1
Chemical compositions of OPC, SF, SAC and CCW.

Constituent (wt%)	SiO_2	Fe_2O_3	Al_2O_3	CaO	CO_2	MgO	SO_3	K_2O	Na_2O	LOI
OPC	20.40	3.38	4.70	64.70	–	0.87	1.89	0.49	0.33	3.24
SF	92.90	0.08	2.49	0.84	–	0.99	0.36	1.64	0.28	1.04
SAC	8.11	0.78	27.56	36.19	–	1.05	14.47	0.48	0.11	11.76
CCW	0.29	0.07	0.11	54.93	42.08	2.11	0.30	–	–	0.11

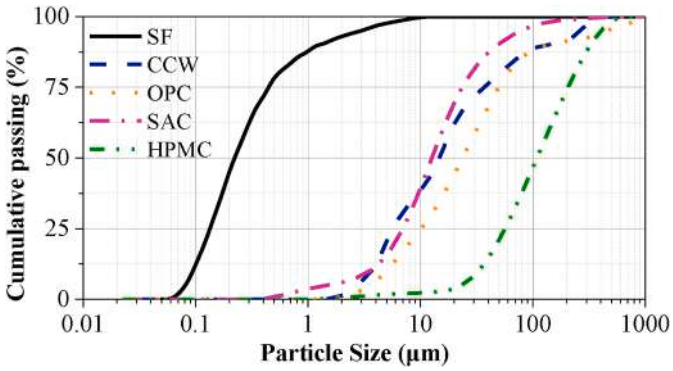

Fig. 1. Particle size distributions of silica fume (SF), calcium carbonate whisker (CCW), ordinary Portland cement (OPC), sulfoaluminate cement (SAC) and hydroxypropyl methyl cellulose (HPMC).

formwork, inside which conventional steel reinforcement or prestressed tendons can be post-installed, and then concrete can be poured inside. Although, this approach does not utilize the full capabilities of 3DCP (i.e. printing a structure rather than printing a formwork); however, this method has its own benefits including reduction in construction waste, time and cost, especially when formworks with complex geometries are needed. Manufacture of such bespoke formworks with conventional materials/production processes would be very challenging and costly, if not impossible. For example, Vantyghem et al. [12] reported manufacture and testing of a 3D printed post-tensioned concrete girder designed by topology optimization. In 2019, researchers at ETH Zurich 3D printed nine 2.7 m high hollow concrete columns with very complex geometry and surface texture, and conventional steel reinforcement cages were then installed in the printed columns, followed by concrete pouring [13]. In another study, Salet et al. [14] designed and tested a 3D printed concrete bridge by printing a group of hollow concrete segments and post-installation of prestressed tendons. However, there is still very limited research on the performance of components made using a 3D printed permanent concrete formwork.

This study aims to investigate the 3D concrete printing of permanent formwork for concrete column construction. At first, several mixtures were designed to identify an optimum 3D printable mixture for production of permanent concrete formwork. The rheological properties, structural build-up, mechanical strength and printing performance of different mixtures were systematically characterized. Subsequently, the number of failure layer of the optimum mixture due to plastic yielding was predicted using the Kruger et al. [15]'s thixotropy model, and the predictions were compared with the experimental results. Finally, the overall stability of the 3D printed permanent concrete formwork and the influence of steel reinforcement ratio on the bearing capacity of the concrete columns were investigated.

2. Experimental program

2.1. Materials

In this study, the cementitious binder was composed of ordinary Portland cement (OPC), sulfoaluminate cement (SAC) and silica fume (SF). Type II 52.5 OPC, complied with Chinese standard GB175-2007, with a 28-day compressive strength of 52.8 MPa was used. Undensified SF of Grade 955 complied with Chinese standard GB/T 27690-2011was used. SAC has many excellent characteristics, such as high early strength, good dimensional stability, and low CO_2 emissions as compared to OPC. In this study, the SAC with a 1-day compressive strength of 46.4 MPa was used as OPC accelerator to enhance the aluminate hydration reactions and improve the structural build-up [16,17]. The chemical compositions of the OPC, SF, and SAC are given in Table 1. Hydroxypropyl methyl cellulose (HPMC) with viscosity value of 38000–42000 mPa.s was used as a viscosity modifying agent. The particle size distributions of SF, OPC, SAC, and HPMC are plotted in Fig. 1.

A combination of river sand (with a specific surface area of 0.101 m^2/g) and fine silica sand (with a mean size of 150 μm) was used as the fine aggregate in this study. The mass ratio of the river sand to the fine silica sand was 3:1. The fineness modulus and maximum size of the fine aggregate were 2.51 and 1 mm, respectively. A polycarboxylate (PCE)-based superplasticizer with a water-reducing rate of 45% by weight and a solid content fraction of 20% was used to lower the water-to-binder ratio (W/B).

Furthermore, short polyethylene (PE) fibers (6 mm long and with an aspect ratio of 500) and calcium carbonate ($CaCO_3$) whisker (CCW) were employed as the reinforcement materials in order to reduce the risk of shrinkage of printing materials and to enhance micro mechanical performance to some extent. The particle size distribution and chemical composition of CCW are also presented in Fig. 1 and Table 1, respectively. The physical properties of the PE fiber and CCW, provided by their manufacturers, are summarized in Table 2. Fig. 2 presents scanning electron microscope (SEM) images for the SAC, SF, CCW and PE fiber used in this study.

2.2. Mixtures proportions and mixing

As shown in Table 3, nine mixtures were designed to study the effect of water content and HPMC content. Three different W/B (0.27, 0.29 and 0.31) and three different amounts of HPMC (0, 0.0003 and 0.0006 by mass of the binder) were used. The amount of the PE fiber and CCW in all mixtures were kept constant.

All mixtures were prepared in a 40 L planetary mixer. The OPC, SF, SAC, CCW and fine aggregates were first dry mixed for 2 min at 140 rpm. Then, water and SP were gradually added to the mixer and the fresh materials were mixed at 140 rpm for 3 min. Once a consistent and flowable mixture was reached, the HPMC powder was added to the fresh

Table 2
Physical properties of PE fiber and CCW.

Material	Density ρ (g/cm^3)	Tensile strength f_{tf} (GPa)	Elastic modulus E_f (GPa)	Length L_f (mm)	Diameter d_f (μm)	Aspect ratio L_f/d_f
PE fiber	0.97	3.0	116	6	24	250
CCW	2.8	3000–6000	410–710	0.02–0.03	0.5–2	20–60

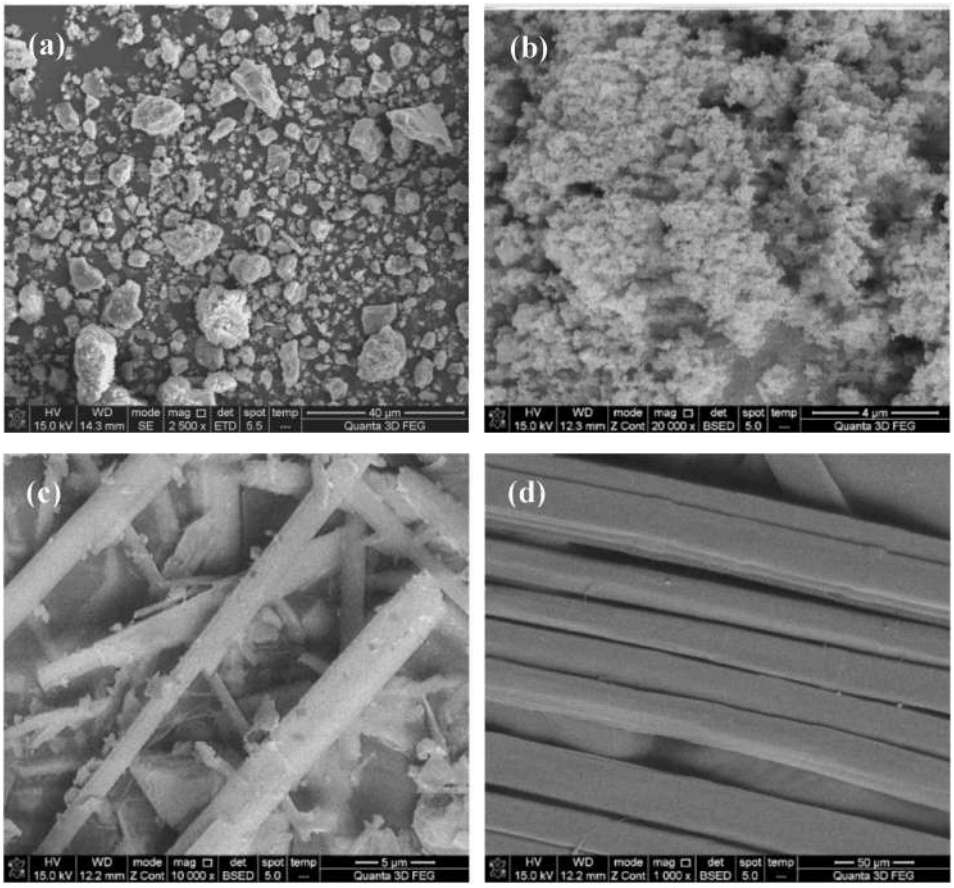

Fig. 2. SEM micrographs of (a) SAC (b) SF (c) CCW and (d) PE fiber.

Table 3
Mix proportions of the 3D printable materials.

Mix No.	OPC	SAC	SF	F. Agg.	Water	SP	HPMC	CCW	PE fiber
M1	0.82	0.03	0.15	0.8	0.27	0.001	0.0000	0.1	0.001
M2	0.82	0.03	0.15	0.8	0.29	0.001	0.0000	0.1	0.001
M3	0.82	0.03	0.15	0.8	0.31	0.001	0.0000	0.1	0.001
M4	0.82	0.03	0.15	0.8	0.27	0.001	0.0003	0.1	0.001
M5	0.82	0.03	0.15	0.8	0.29	0.001	0.0003	0.1	0.001
M6	0.82	0.03	0.15	0.8	0.31	0.001	0.0003	0.1	0.001
M7	0.82	0.03	0.15	0.8	0.27	0.001	0.0006	0.1	0.001
M8	0.82	0.03	0.15	0.8	0.29	0.001	0.0006	0.1	0.001
M9	0.82	0.03	0.15	0.8	0.31	0.001	0.0006	0.1	0.001

Note: OPC: ordinary Portland cement; SAC: sulfoaluminate cement; F. Agg.: fine aggregate; SF: silica fume; CCW: calcium carbonate whisker; SP: Superplasticizer; PE fiber: polyethylene fiber; HPMC: hydroxypropyl methyl cellulose. All numbers are mass ratios of the binder (OPC+SF+SAC) mass, except the CCW content (volume fraction).

material and the mixing was continued for 1 min at 140 rpm. Subsequently, the PE fibers were gradually added to the mixer and mixed for 1 min at 140 rpm to achieve a uniform fiber dispersion. Lastly, the fresh composite was mixed for 1 more min at 420 rpm to complete the mixing procedure.

2.3. Testing procedures

2.3.1. Rheological measurement

Rheological properties have crucial effects on the printability and printing quality of the cement-based composite materials. In order to have the same material state and history, all fresh mixtures were subjected to a rest duration of 10 min before starting the rheological measurements. Subsequently, the stress growth test was performed to obtain the evolution of static yield stress and to investigate the effect of different factors on the rheological behavior. The rheological properties of the fresh mixtures were measured at ambient temperature (23 °C ± 1 °C) using a Brookfield RST-SST rheometer equipped with a four-bladed vane with 10 mm diameter and 20 mm height (Fig. 3(a)). Fig. 3(b) presents the simplified schematic diagram of the shear stress development. Three specimens were prepared and tested for each mixture. The total duration of the stress growth test was 2 min, and each fresh specimen was subjected to a low constant rotational speed (0.2 s^{-1}) and the static and dynamic yield stresses were recorded. In addition, the difference between the static yield stress and the dynamic yield stress was used to evaluate thixotropy [18,19]. In this study, a relatively low shearing speed of 0.2 s^{-1} was applied to reduce the viscous effect, because a higher shearing speed may result in segregation of the constituents and lead to over estimation of the yield stress [20,21].

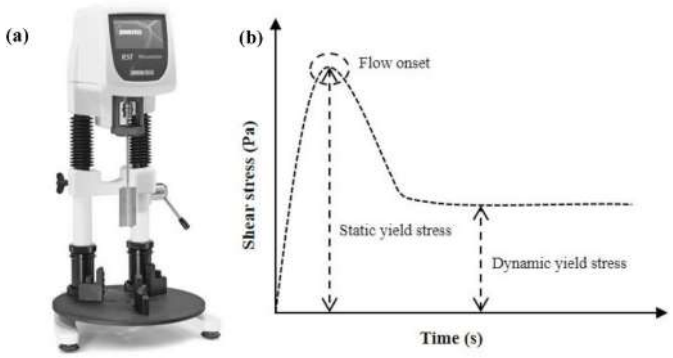

Fig. 3. (a) Brookfield RST-SST rheometer for stress growth test and (b) Shear stress development under constant shear rate of 0.2 s^{-1}.

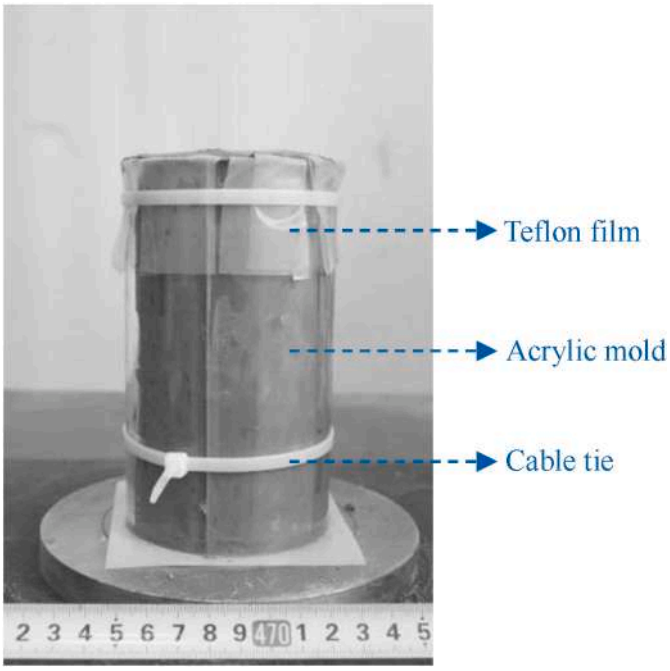

Fig. 4. Cylindrical specimen preparation for measurement of green strength.

2.3.2. Assessment of structural build-up

After extrusion, printed filaments should have enough structural build-up to retain their shapes and do not have excessive deformations due to weight of subsequent layers printing on top of them. In this study, following [22–24], unconfined uniaxial compression tests (UUCTs) were performed to investigate the green strength of each mixture. Acrylic molds with a height of 140 mm and an inner diameter of 70 mm were used to prepare the test specimens (Fig. 4). The cylindrical mold was composed of two parts, linked together by cable ties. Teflon film was used to reduce the cohesion between the material and the mold. After casting of the cylindrical specimens, they were left in the molds for 10 min (to be at rest for 10 min similar to the fresh materials used for the rheological tests), and then were demolded for testing. It should be noted that before the UUCTs, the slump of each cylindrical specimen was measured. The slump S (mm) was calculated based on the following equation:

$$S = h_m - h_d \tag{1}$$

where h_m is the mold height (mm) and h_d is the height of specimen after removing the mold (mm). If S > 15 mm or unstable collapse occurred (i.e. large deformation occurred), the UUCT was not conducted for that mixture.

Fig. 5(a) shows the setup for the UUCT. For each mixture, 16 cylindrical specimens were prepared and tested for resting times of 10, 30, 60 and 90 min; where four specimens were tested for each resting time. Following [22], a servo–hydraulic universal testing machine was employed to conduct the compression test at a rate of 30 mm/min. A digital camera was used to record the whole test process, and then ImageJ software was used to calculate the transverse deformation of each specimen. The mean diameter ($D_{t,mean}$ = average of D_1 to D_5) was used as the transverse diameter of the specimen at each time during the test (see Fig. 5(b)). The vertical strain (ε_t) at every moment was calculated by dividing the vertical displacement of the specimen at each time (u_t) by the height of the specimen after removing the mold (h_d). The vertical displacement was extracted from the photographs taken during the tests. The axial stress (σ_t) at every moment can be obtained based on the recorded axial force (F_t), and the stress-strain curves were plotted. The ε_t, σ_t and $D_{t,mean}$ were calculated using the following equations:

$$D_{t,mean} = \frac{\sum_{i=1}^{5} D_i}{5} \tag{2}$$

$$\sigma_t = \frac{F_t}{\pi \times \left(\frac{D_{t,mean}}{2}\right)^2} \tag{3}$$

$$\varepsilon_t = \frac{u_t}{h_d} \times 100\% \tag{4}$$

2.3.3. Mechanical properties measurement

In this study, the compressive and flexural strengths of each mixture were measured using the conventionally mold-cast specimens at 28 days after casting. The fresh materials were cast into prismatic steel molds (40 mm × 40 mm × 160 mm). After 24 h, the specimens were demolded and stored in the laboratory condition (23 °C ± 1 °C and 95 ± 5% relative humidity) until the day of testing. Three specimens for each mix were used for the bending and compression tests. The mechanical test was performed using a fully automatic testing machine with a load capacity of 300 kN. At first, the bending tests were conducted. Then, the compression tests were conducted on the 40 mm cube specimens extracted from the prisms after completion of the flexural tests.

Fig. 5. (a) Setup for the unconfined uniaxial compression test and (b) photograph of a fresh specimen during image analysis.

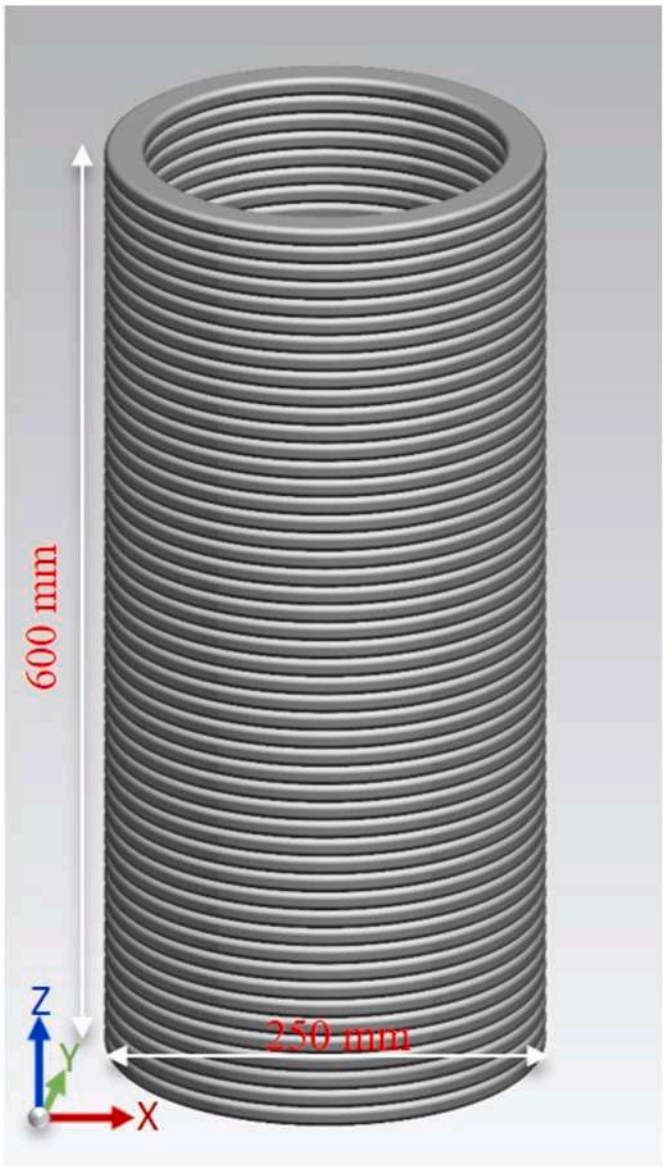

Fig. 6. 3D model of the hollow column.

Table 4
Summarized printing parameters as input parameters for the model.

Printing parameter	Value
h_1	12 mm
w_1	25 mm
l_p	785.4 mm
v	34.1 mm/s
Aspect ratio (h_1/w_1)	0.48
F_{AR}	1.41

Note: h_l is defined as the layer height (mm); w_l is defined as the layer width (mm), l_p is the constant path length of each layer (mm), v the printing speed (mm/s) and F_{AR} is the strength correction factor.

2.3.4. Structural failure prediction

According to the results obtained in Sections 2.3.1, 2.3.2 and 2.3.3, an optimum mixture for 3DCP was selected, and then its buildability performance was investigated. Obviously, it is useful to predict the structural failure of cementitious materials before printing a structure, as it can help for quality control of materials and the selection of the printing parameters. Recently, Kruger et al. [15] developed a rheological parametric model that can be used for the prediction of structural failure of 3D printed concrete, which mainly accounts for plastic collapse model. In order to conduct the experimental verification using Kruger et al. [15] model, printing parameters and material's rheological parameters should be obtained first. In this study, a circular hollow column measuring 250 mm in diameter and 600 mm in height (see Fig. 6) was continuously printed at 34.1 mm/s until failure and the result was compared with the model's prediction. The printed circular hollow column was used as the permanent formwork to fabricate composite columns in Section 2.3.5. Specifically, the printing parameters used as input parameters in this model are summarized in Table 4.

Furthermore, based on these printing parameters, the stress growth tests on the optimum mixture at different resting times (0, 10, 20, 30, 40, 90, 120 and 1200 s) were conducted to obtain the relevant rheological parameters ($\tau_{S,i}$, $\tau_{D,i}$, R_{thix} and A_{thix}). Here, $\tau_{S,i}$ is initial static yield shear stress of the material (Pa), $\tau_{D,i}$ is initial dynamic yield shear stress of the material (Pa), R_{thix} is short term re-flocculation rate (Pa/s) and A_{thix} is structuration rate (Pa/s). Finally, the parameters obtained were substituted into the model to predict the number of printed layers before failure (N_L), which can be expressed in the form of the following two equations based on limited conditions:

$$N_L = -\left[\frac{\tau_{D,i}}{\left(\frac{R_{thix}\cdot l_p}{v}\right) - \left(\frac{\rho\cdot g\cdot h_1}{2\cdot 10^3\cdot F_{AR}}\right)}\right] \quad (5)$$

$$N_L = -\left[\frac{\tau_{S,i} + \left(\frac{A_{thix}\cdot\left(\tau_{D,i}-\tau_{S,i}\right)}{R_{thix}}\right)}{\left(\frac{A_{thix}\cdot l_p}{v}\right) - \left(\frac{\rho\cdot g\cdot h_1}{2\cdot 10^3\cdot F_{AR}}\right)}\right] \quad (6)$$

Further details regarding the testing procedure and the parameter calculation formulas can be found in Refs. [15,25].

2.3.5. Manufacture and compression test of composite columns using printed concrete as permanent formwork

Based on the results of experimental verification, the number of failure layer of the optimum mixture can be determined. In turn, the results can guide the quality control of materials (e.g. hydration rate control by addition of retarders, etc.) and the setting of printing parameters (e.g. changing nozzle size and printing speed, etc.). Fig. 7 shows the 3D concrete printer used in this study having the print area of 3 m × 2 m and the height of 3 m. The cone-shape extrusion device contained compression section with a gradual groove depth mixing screw and forming section with an opening of Ø20 mm.

At present, the assembly of structural components is the development trend of engineering construction. Assembly of 3D printed components is a beneficial supplement to the assembly of structure owing to significant benefits in terms of customization, making members with complex shapes, ease of transport and segmental assembly on site. Considering that the printed permanent formwork has a number of failure layer when printing, it is necessary to assemble the 3D printed composite column in sections when the column is fabricated in field. Fig. 8 shows the schematic illustration of the assembly of a 3D printed composite column. Since the structure is assembled in segments, reinforcement area should be reserved at the splicing region, the reinforcement in this area can be connected by mechanical connection or manual overlapping, and the safety and reliability of the structure can be guaranteed by seam grouting.

In order to study the performance of 3D printed permanent formwork and the influence of reinforcement ratio on the bearing capacity of the composite columns, three composite columns were designed as shown in Table 5. Three cast-in-place columns with the same reinforcement ratios were also designed for comparison purposes (see Table 5). Fig. 9(a) shows a composite column, in which the printed

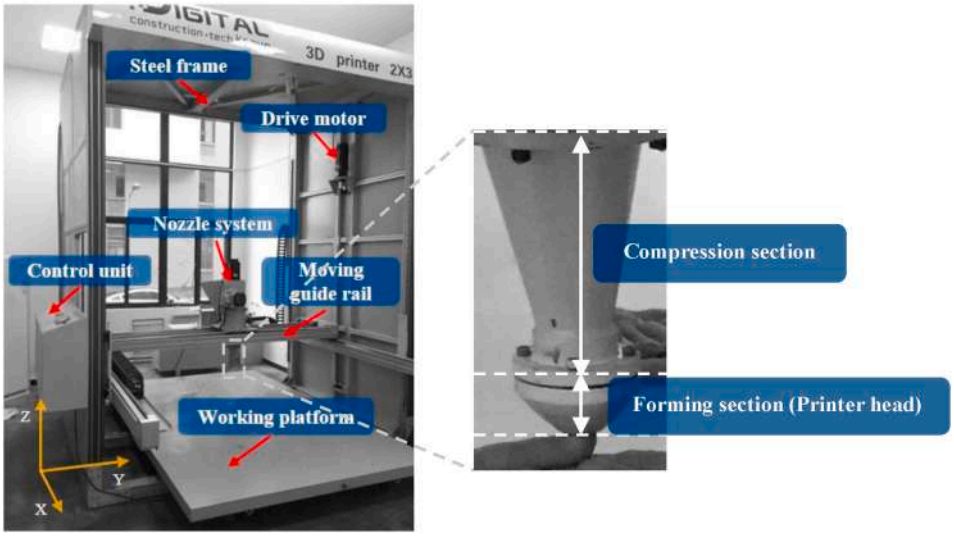

Fig. 7. 3D concrete printer used in this study.

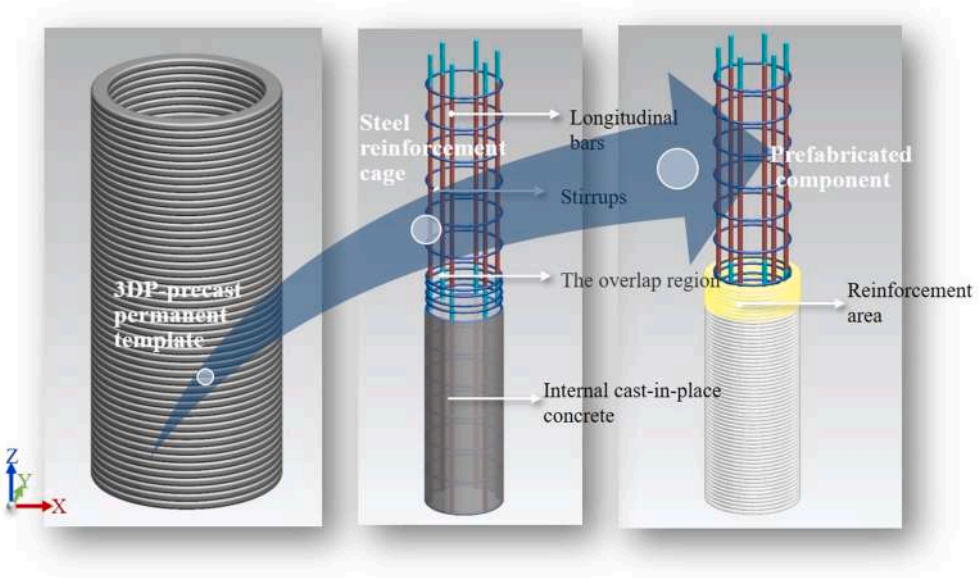

Fig. 8. Schematic representation of the assembly of a 3D printed composite column.

Table 5
Reinforcement detailing of composite column specimens.

Specimen ID	Reinforcement detailing	
	Stirrup	Longitudinal bar
3DP-PJ0	–	–
Cast-PJ0	–	–
3DP-PJ1	C8@100 mm	6C14
Cast-PJ1	C8@100 mm	6C14
3DP-PJ2	C8@100 mm	8C14
Cast-PJ2	C8@100 mm	8C14

concrete was used as the permanent formwork. It should be noted that the diameter and height of both types of columns (i.e. the cast-in-place columns and the composite columns) were 250 mm and 500 mm, respectively.

The procedure for manufacture of the composite columns was as follows: (1) After completion of the mixing procedure (as per Section 2.2) the fresh materials were placed at rest for 10 min before being extruded. This was to ensure the fresh material used for printing the permanent formwork had the same material state and history to the fresh material used for the rheological measurements and UUCTs. (2) The permanent formwork was then printed and stored in the laboratory condition (23 °C ± 1 °C and 95 ± 5% relative humidity) for 24 h (3) Subsequently, the pre-made reinforcement cage was placed inside the permanent formwork. (4) The conventional concrete was then cast into the permanent formwork and the composite column specimen was stored in the laboratory condition (23 °C ± 1 °C and 95 ± 5% relative humidity) for 28 days before testing. It should be noted that the average 28-day cubic compressive strength of the printed concrete and the cast-in-place concrete were 40 MPa and 30 MPa, respectively.

Each column specimen was tested under pure axial loading using a hydraulic testing machine. The test data was recorded by a data acquisition instrument. The test loading device and test setup are shown in Fig. 10. In the axial direction of the circular short column, two Linear Variable Differential Transducers (LVDTs) with a measuring range of 100 mm were mounted on the bearing plate to measure the longitudinal displacement of the composite column, and an electric resistance strain

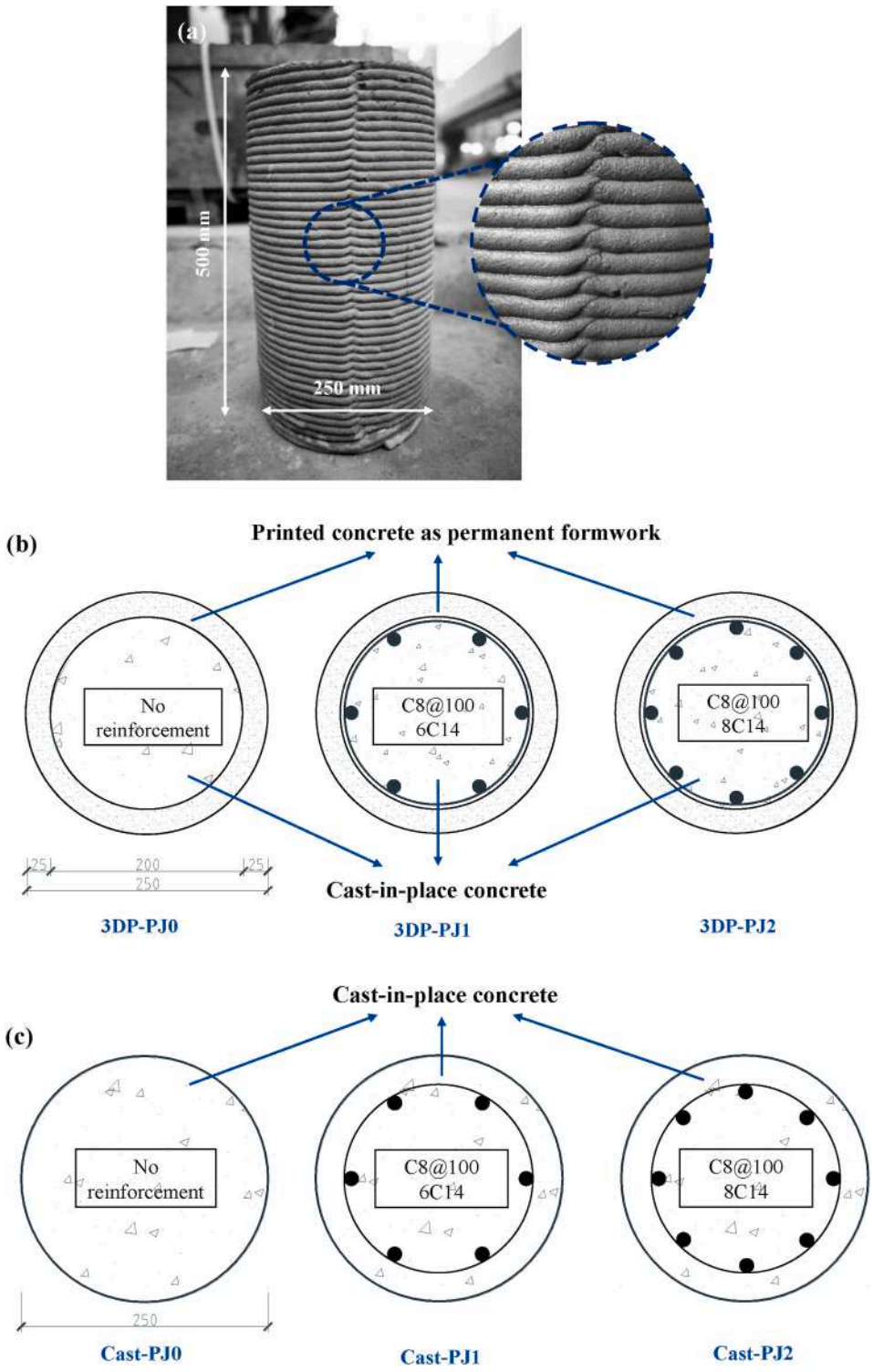

Fig. 9. (a) The composite column with using 3D printed concrete as permanent formwork, (b) Cross sections and reinforcement details of the composite columns, and (c) Cross sections and reinforcement details of the cast-in-place columns (unit: mm).

gauge was placed at the mid-height on both sides of the column to observe the displacement and strain growth in the process of compression.

According to the relevant literature [26,27], the loading scheme of this test was as follows:

(1) Pre-loading: in the preloading stage, the preload was about 15% of the calculated ultimate load, and then the specimen was unloaded, and the data collection was started again.
(2) Regular loading: from the beginning of the loading to 80% of the predicted ultimate bearing capacity, the loading increment was 1/10 of the predicted ultimate bearing capacity. At each loading interval, the load and the corresponding longitudinal displacement values were recorded, and then the loading was increased.

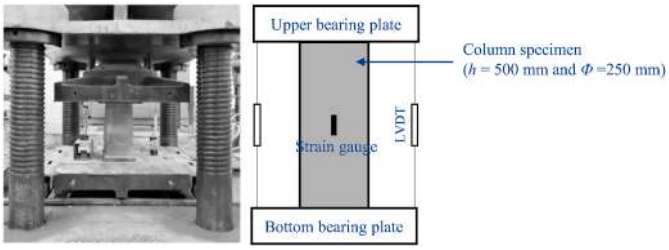

Fig. 10. Setup for testing of concrete column specimens.

When the applied load reached to 80% of the ultimate bearing capacity, the loading increment was reduced to 1/20 of the predicted ultimate bearing capacity. When the specimen was loaded close to the ultimate bearing capacity, it was loaded continuously to collect the test data under the ultimate state. When the load reached to the ultimate bearing capacity, the loading was continued and the load values were recorded until the specimen had great deformation, and the load value dropped to 80% of the ultimate bearing capacity. When the load-deformation curve had obvious decline section, the test was stopped.

3. Results and discussions

3.1. Stress growth test results

The shear stress versus time results of all mixtures with different W/B and HPMC contents are presented in Fig. 11. Generally speaking, the evolution of shear stress of each mixture was similar, first increased and then decreased to an equilibrium value, but the changing range of stress value was quite different depending on the W/B and HPMC content. The peak value of shear stress in Fig. 11 was noted as the static yield stress of cementitious materials (i.e. the stress necessary to initiate flow from at rest stage).

The static yield stress and corresponding thixotropy values of each mix are summarized in Table 6. M1 had a certain thixotropy, however its static yield stress was low, which would lead to lower shape-retention-ability and load bearing capacity. M2 and M3 without the addition of HPMC showed approximately no thixotropy, owing to their relatively high W/B ratios. M4, M5 and M6 showed thixotropy in different degrees, among which M4 showed the largest value of thixotropy. Comparing M1 with M4 clearly showed that the addition of a small amount of HPMC greatly improved the static yield stress of the fresh mixture. The viscosity-enhancing effect of HPMC can be explained by these two mechanisms: (1) connecting cement particles [28,29] and (2) combining free water [30,31].

M7 (with the HPMC content of 0.0006 and the W/B ratio of 0.27) showed the maximum static yield stress and the largest thixotropy, which is very beneficial for the buildability requirement of 3DCP. Here, in terms of the yield stress and thixotropy, M7 can be considered as the optimum mixture, and the assessment of its structural build-up is presented in Section 3.2. It is interesting to note that the static yield stress and the thixotropy of M8 and M9 were much lower than those of M5 and M6. According to Roussel et al. [32] and Marchon et al. [19], different chemical admixtures can generate a competitive adsorption on the surface of cement particles, which in turn will influence their performances in the cement-based materials. In the mixtures investigated in this study, the PCE-based SP and HPMC may also have competitive adsorption relationship [33–35]. More studies are needed to investigate the adsorption and desorption of PCE-based SP and HPMC. In summary, when the W/B was 0.27 and the HPMC content was 0.0006, the mixture showed superior thixotropy that is desirable for 3DCP.

Table 6
Static yield stress and corresponding thixotropy value of each mix.

Mix No.	Static yield stress (Pa)	Corresponding thixotropy value	HPMC content	W/B
M1	382.3	193.0	0.0000	0.27
M2	28.0	1.6	0.0000	0.29
M3	26.2	0.7	0.0000	0.31
M4	1276.6	717.1	0.0003	0.27
M5	1087.0	606.4	0.0003	0.29
M6	695.9	404.2	0.0003	0.31
M7	2622.1	2022.1	0.0006	0.27
M8	644.0	311.5	0.0006	0.29
M9	417.0	58.1	0.0006	0.31

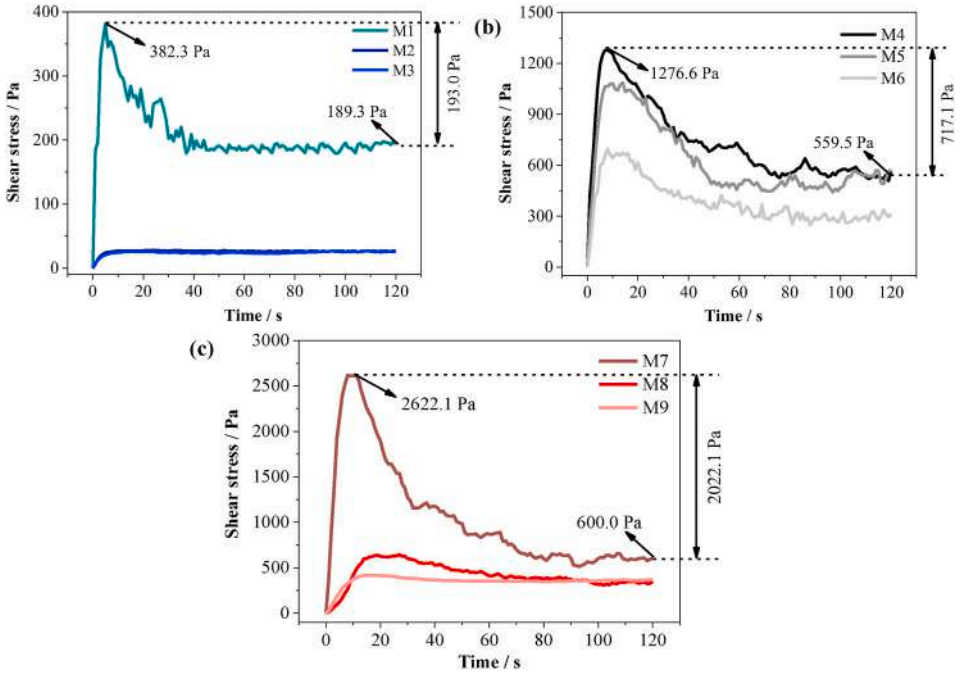

Fig. 11. Shear stress vs time results for mixtures with different W/B. (a) HPMC content = 0, (b) HPMC content = 0.0003 and (c) HPMC content = 0.0006.

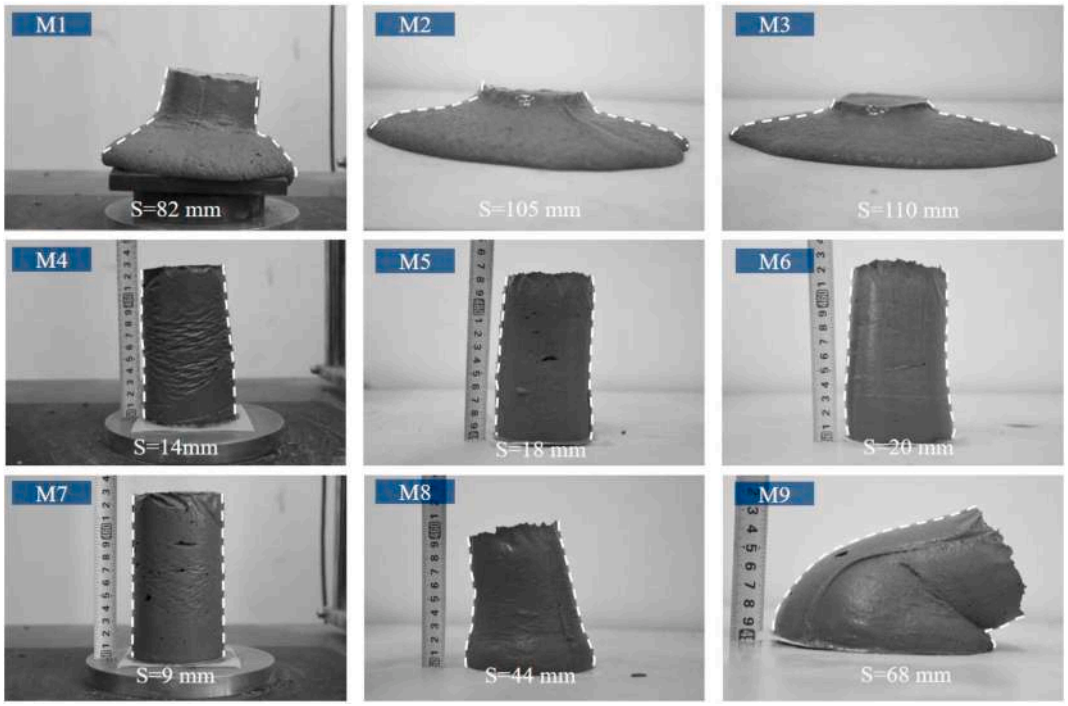

Fig. 12. Shape-retention-ability and slump values (S) of different fresh specimens after demolding.

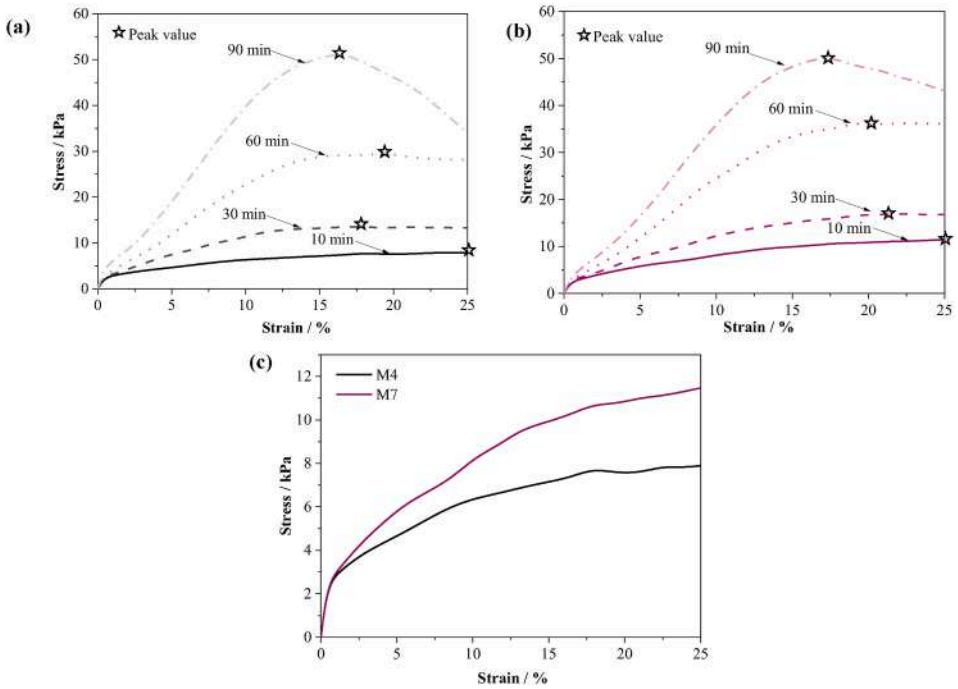

Fig. 13. Stress-strain curves of unconfined uniaxial compression tests on the fresh specimens at different resting times of t = 10, 30, 60 and 90 min: (a) M4, (b) M7 and (c) M4 and M7 at resting time of t = 10 min.

3.2. Structural build-up results

Fig. 12 shows the shape-retention-ability of each cylindrical specimen after demolding. As shown in this figure, M1, M2 and M3 without using any HPMC showed large deformations under self-weight. The slump values measured for M1, M2 and M3 were 82, 105 and 110 mm, respectively. Moreover, the failure pattern of M1, M2 and M3 was plastic collapse. When the HPMC content was 0.0003, the shape-retention-ability of the specimens was greatly improved. The slump values of M4, M5 and M6 were 14, 18 and 20 mm, respectively, decreasing by 83%, 83% and 82% with respect to M1, M2 and M3, respectively. However, a certain inclination pattern was observed in these specimens, i.e. plastic deformation due to low material's rigidity. When the addition of HPMC was increased to 0.0006, M7 showed the best shape-retention-ability with a relative low slump value of 9 mm, as expected. However, M9 showed large collapse and M8 showed elastic buckling. According to

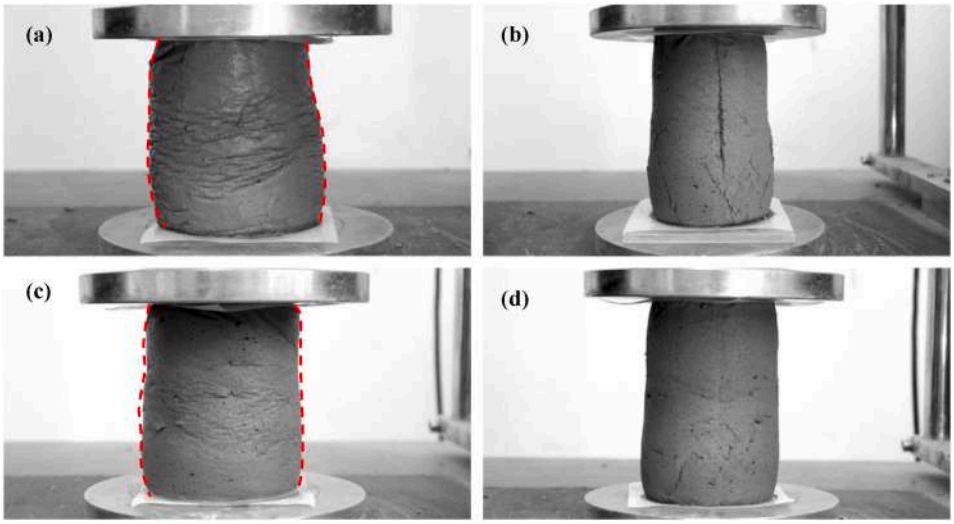

Fig. 14. Typical failure modes of fresh specimens (a) M4 specimen at t = 10 min, (b) M4 specimen at t = 90 min, (c) M7 specimen at t = 10 min and (d) M7 specimen at t = 90 min.

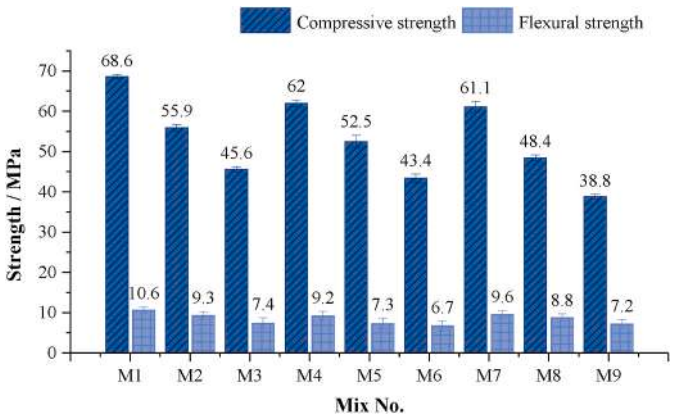

Fig. 15. Average compressive and flexural strengths of different mixtures.

Fig. 12, it can be concluded that only M4 and M7 had a slump value of less than 15 mm, and M7 showed the best shape-retention-ability with the HPMC content of 0.0006 and the W/B of 0.27. Additionally, the shape-retention-ability of the specimens with the same W/B ratio of 0.27 was enhanced by increasing the dosage of HPMC. However, the shape-retention-ability of other specimens with the same W/B of 0.29 and 0.31 were enhanced first and then decreased by increasing the dosage of HPMC.

The UUCTs were only performed on the fresh specimens of M4 and M7, as they showed the slump value of less than 15 mm. Fig. 13 shows the stress-strain curves of M4 and M7 at different resting times.

As shown in Fig. 13(a) and (b), in both M4 and M7 the strength and stiffness as well as the peak stress point increased as the resting time increased. The peak stress values of M7 (with HPMC = 0.0006) were higher than those of M4 (with HPMC = 0.0003) at resting times of t = 10, 30, and 60 min, which means M7 had a faster early strength development rate as compared to M4. However, at resting time of t = 90 min, the peak stress of M4 (51.5 kPa) was 1.3 KPa higher than that of M7 (50.2 kPa). It is obvious in Fig. 13(c) that M7 (with peak stress value of 11.7 kPa) had higher green strength development rate at resting time of t = 10 min than that of M4 (with peak stress value of 8.0 kPa), which contributed to superior shape-retention-ability of M7 to M4. Fig. 15 shows the typical failure modes of the fresh specimens of M4 and M7. When the specimen was at the early age (t = 10 min), both M4 and M7 specimens showed 'barreling' effect to a certain extent due to having a relatively low stiffness, see Fig. 14(a) and (c). However, when the specimen was at the older age (t = 90 min), both M4 and M7 specimens showed a distinct shear failure plane, see Fig. 14(b) and (d). Because of the higher green strength, the 'barreling' effect and shear failure plane in M7 were less pronounced than M4.

3.3. Mechanical properties

The average 28-day compressive and flexural strengths of each mix are depicted in Fig. 15. For the same HPMC content, the compressive and flexural strengths of the specimens decreased with the increase of W/B from 0.27 to 0.31. Moreover, for the same W/B, the compressive strength of the specimens decreased with the increase of HPMC content from 0 to 0.0006. On the other hand, the flexural strength of the specimens decreased first and then slightly increased as the HPMC content increased from 0 to 0.0003 and then to 0.0006, but the rate of decrease was higher than the rate of increase. Therefore, it can be said that the addition of HPMC reduces the compressive and flexural strengths of the material to a certain extent. The possible reason for the HPMC effect on the mechanical properties can be explained as follows:

On the one hand, the addition of HPMC can strengthen the microstructure of matrix with reducing the number of micro-cracks and controlling the shrinkage and cracking in the hardened state. This is because of reducing the rate of water evaporation owing to the water-retention ability of HPMC, thereby improving the mechanical strength of cement-based materials [36–38]. On the other hand, HPMC has the function of containing entrained air, which will increase the porosity

Table 7
Summary of the yield stress results obtained for the optimum mixture (M7).

Parameter	Resting time between tests							
	Initial	10 s	20 s	30 s	40 s	90 s	120 s	20 min
Static yield stress (Pa)	2622.1	863.2	943.4	1020.1	1165.9	1751.8	1996	4339.5
Dynamic yield stress (Pa)	600	308.5	311.3	290.6	312.3	517.1	490.4	764.1

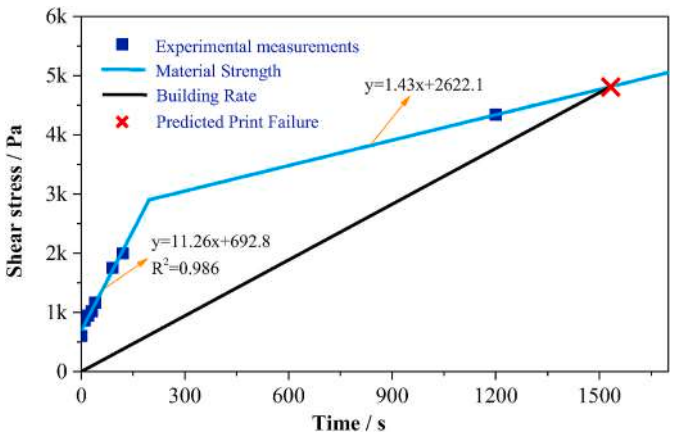

Fig. 16. Visual representation of the material strength, building rate of the optimum 3D-printable mixture (M7) and the predicted print failure.

and have a negative impact on the material strength [39,40]. In this study, when the HPMC content increased from 0 to 0.0003, the weakening effect of the HPMC was dominant. When the HPMC content increased from 0.0003 to 0.0006, the weakening effect of HPMC was still dominant, while the gap between the strengthening effect and the weakening effect was reduced.

3.4. Structural failure prediction results

The yield stress results obtained for the optimum mixture (M7) are summarized in Table 7. The obtained data, including the dynamic yield stress at zero resting time and the static yield stress at different resting time (10 s, 20 s, 30 s, 40 s, 90 s and 120 s) were plotted against the respective resting times to get the re-flocculation rate (R_{thix}). The static yield stress at zero resting time and at 20 min resting time were plotted against the respective resting times to get the structuration rate (A_{thix}), respectively, as illustrated in Fig. 16. As shown in this figure, the yield strength of material kept increasing (as shown by the blue line) after extrusion. With continuous printing process, the stress in the extruded filament at the bottom increased (as shown by the black line) due to stacking of upper extruded filaments, which is depicted by the building rate development based on the model. Once the static yield strength of the extruded material at the bottom was smaller than the stress built due to filament stacking, the plastic yielding of the bottom filament occurred. After these operations, the initial static yield stress, initial dynamic yield stress, re-flocculation rate and structuration rate are 2622.1 Pa, 600 Pa, 11.26 Pa/s and 1.43 Pa/s, respectively. According to the prediction model, density (ρ) of the fresh material should be obtained. This parameter was obtained by dividing the mass of the known volume of the material by its volume, and the determined value was 2050 kg/m^3. Taking these parameters to the model, the predicted number of failure layer (N_L) was 45, i.e. the printed structure will fail due to plastic collapse after 45 layers. The predicted print failure point is depicted by a red cross in Fig. 16.

As described in Section 2.3.4, a circular hollow column was continuously printed at 34.1 mm/s until failure occurred to verify the thixotropy model. Fig. 17 shows the printed column and the final failure pattern. As shown in Fig. 17(a), the printed column showed good shape-retention-ability and no significant deformation was observed before failure. When the failure occurred, the actual number of failure layer was 49 (see Fig. 17(b)), which was 4 layers more than the predicted number of failure layer (45). The error is relatively small. It should be noted that, right before failure, several cracks were observed at the bottom of the printed column (see the magnified photo in Fig. 17(b)), indicating that the stress at the bottom layers exceeded the material yield strength, which corresponds to failure mechanism of plastic yielding of the bottom layers [15,41,42] that was followed by a secondary instability failure at the top region of the column (see Fig. 17(b)). It can therefore be concluded that it is convenient and accurate to predict the number of failure layer of 3D printed structures due to plastic yielding by the thixotropy model developed by Kruger et al. [15].

3.5. Compression test results of composite columns

Fig. 18 shows the failure pattern of all tested composite column specimens. In the 3DP-PJ0 specimen (with no steel reinforcement), when the load reached 30% of the ultimate load, the first vertical crack appeared near the loading surface, and then the load continued to increase. Many longitudinal cracks appeared at the top and bottom of the column, and an inclined crack appeared in the middle of the column (see Fig. 18(a)). It is worth noting that there was no peeling failure at the printing interval of the formwork. The stress at the interval was not different from other parts of the specimen, showing good integrity of the composite column. With increase in load, several longitudinal cracks near the loading point and the inclined crack began to form the main cracks, and the main cracks gradually widened to a certain extent. Finally, the failure of the column was brittle (see Fig. 18(b)).

For the Cast-PJ0 specimen (with no steel reinforcement), produced by placing the plain concrete in the steel mold, there is no obvious

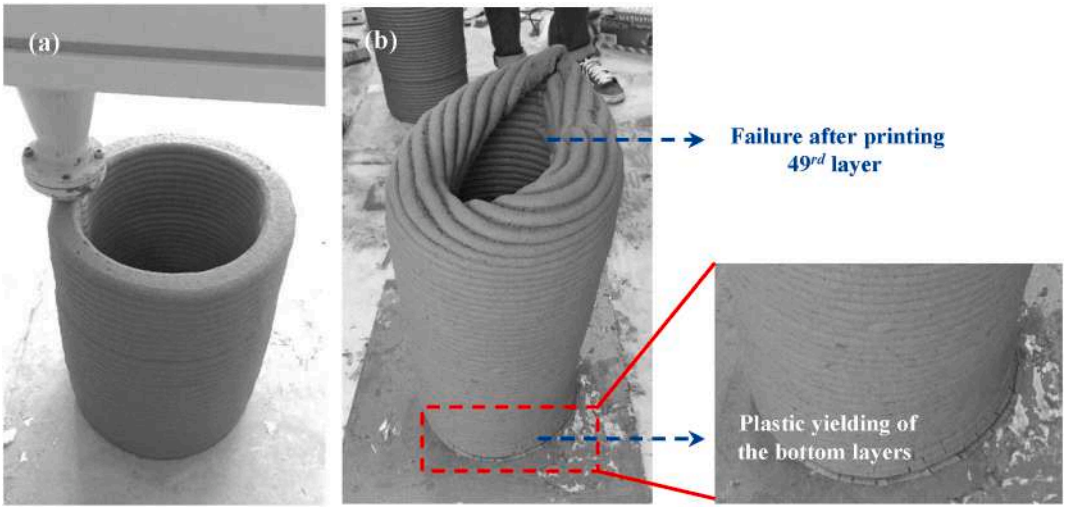

Fig. 17. 3D printing of circular hollow column: (a) During the printing process; (b) Final failure pattern.

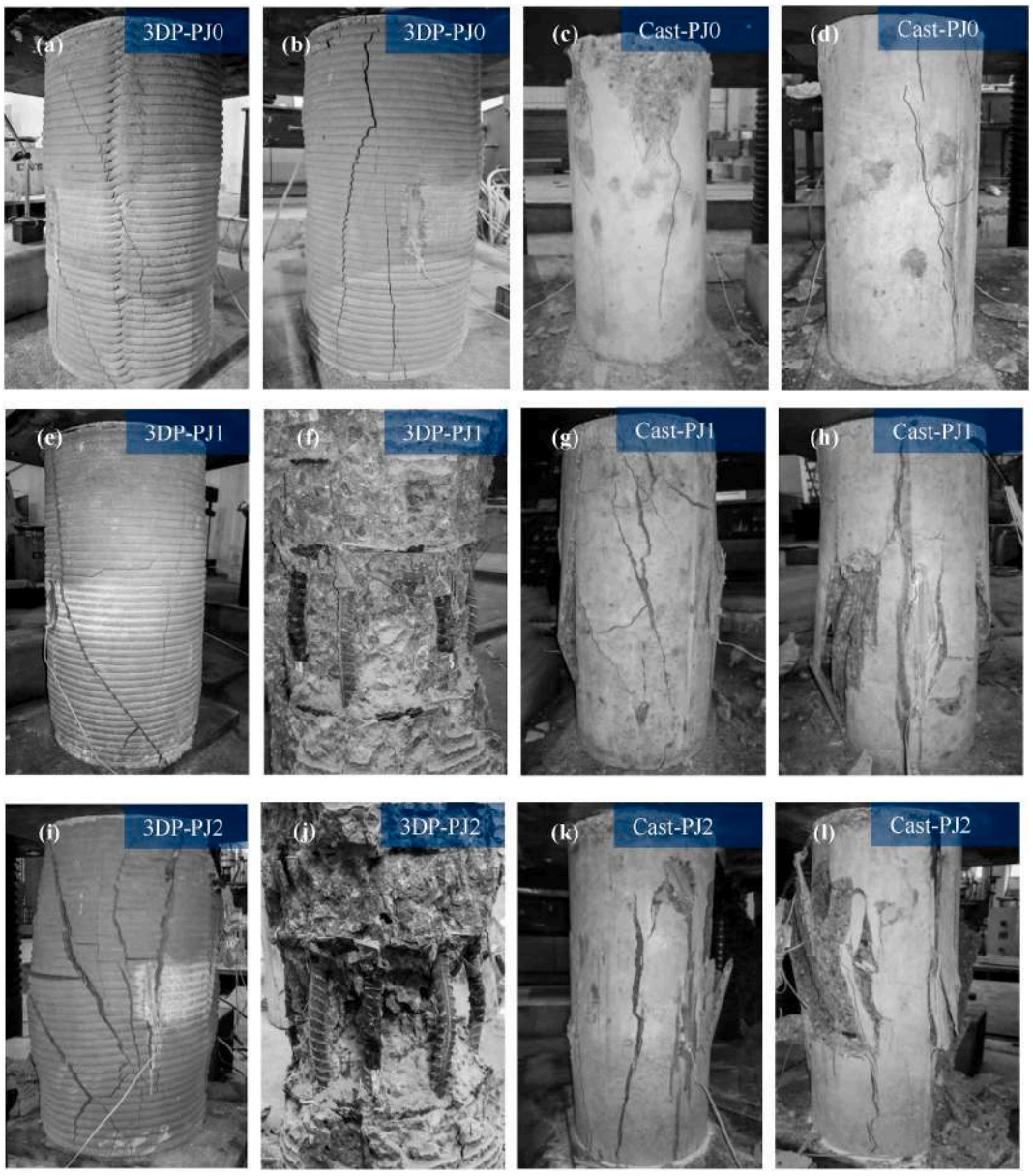

Fig. 18. Failure patterns of all tested composite column specimens (a) Inclined crack of 3DP-PJ0 specimen at printing interval, (b) Final failure pattern of 3DP-PJ0 specimen, (c) Concrete spalling pattern of Cast-PJ1 specimen, (d) Main fracture formation of Cast-PJ1 specimen, (e) Final failure pattern of 3DP-PJ1 specimen, (f) Steel bar buckling of 3DP-PJ1 specimen, (g) Crack connection pattern of Cast-PJ1 specimen, (h) Final failure pattern of Cast-PJ1 specimen, (i) Final failure pattern of 3DP-PJ2 specimen and (j) Steel bar buckling of 3DP-PJ2 specimen, (k) Crack connection pattern of Cast-PJ2 specimen, (l) Final failure pattern of Cast-PJ2 specimen.

phenomenon at the initial stage of loading. When the load reached about 25% of the ultimate load, longitudinal microcracks began to appear near the loading face. As the load continued, the cracks began to increase. When the load increased to about 70% of the ultimate load, many longitudinal cracks at both ends of the column began to connect, which made many edge concretes peeling off (see Fig. 18(c)). At the same time, the microcracks in the middle of the column developed gradually and extended to the loading place to form the main cracks (see Fig. 18(d)). When the load reached the ultimate bearing capacity, the specimen was destroyed instantly.

The 3DP-PJ1 and 3DP-PJ2 specimens were reinforced composite columns. The printing mode of the permanent formwork of these two columns was the same as that of 3DP-PJ0, and the printing interval of each layer was in the same position. At initial stages of loading, the first vertical crack appeared, and then several longitudinal cracks appeared at the top and bottom of the columns, and inclined cracks appeared in the middle of the column. As the load increased, the longitudinal reinforcement between stirrups bended outward and bulged out during the compression process, and the transverse cracks were found near the middle height of the composite column owing to internal tension stress (see Fig. 18(e) and (i)). Subsequently, several longitudinal cracks appeared near the loading surface, and the inclined and transverse cracks began to form main cracks, and the main cracks widened with increase of the load. Finally, the longitudinal reinforcements buckled, and the load didn't increase anymore, meaning the specimens reached the ultimate load. Then, the load decreased slowly, while the longitudinal displacement continued to increase, and the cracks gradually widened. It is worth noting that large area of collapse and peeling of concrete pieces cannot been seen in the specimens. After failure, the damaged permanent formwork and the inside crushed concrete were removed, showing buckling of the longitudinal reinforcement under the axial pressure (see Fig. 18(f) and (j)).

For the Cast-PJ1 and Cast-PJ2 specimens (with the same steel reinforcement as the composite column specimens), the concrete and

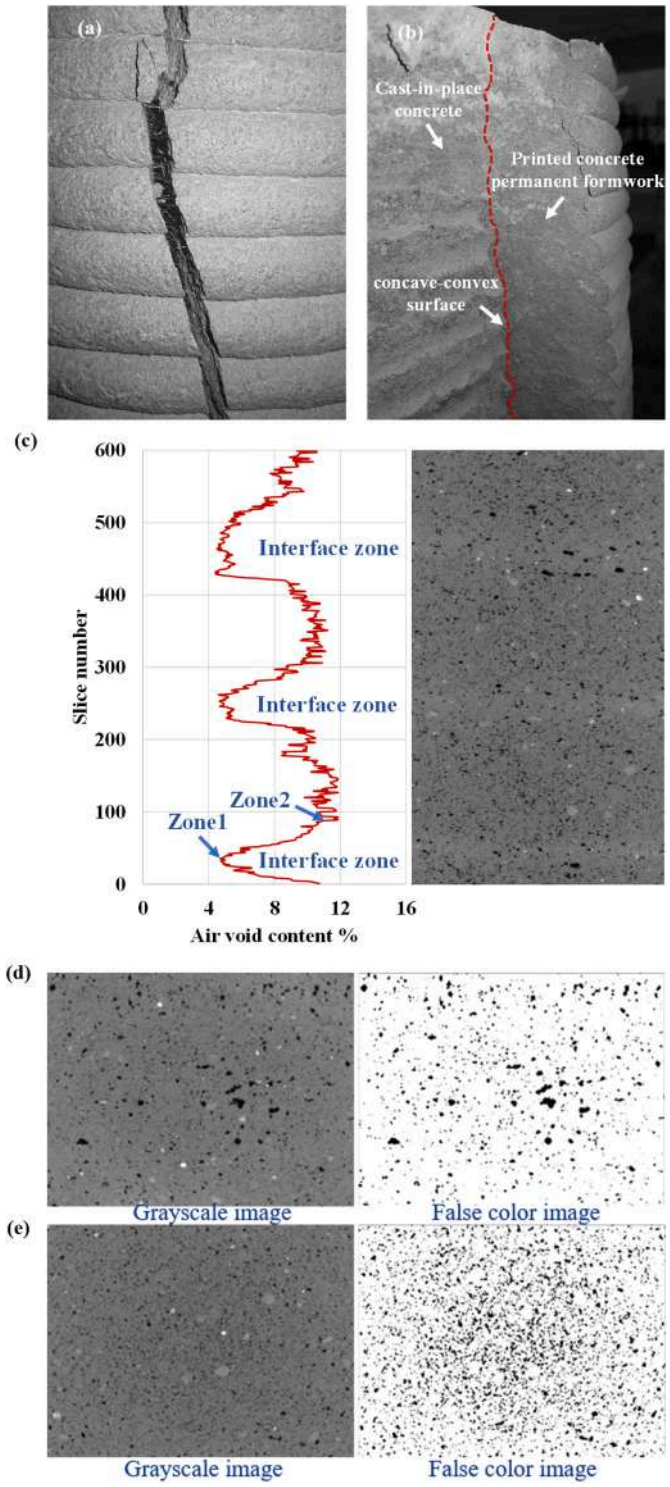

Fig. 19. 3D printed concrete as the permanent formwork of the composite column (a) Crack bridging of fibers, (b) Effect of concave-convex surface on improving bonding properties between the cast-in-place concrete and the printed concrete permanent formwork, (c) Average air void content in the height of sample, (d) The grayscale image and false color image of the interlayer (the interface between layers) from the top view (Zone 1 in (c)), and (e) The grayscale image and false color image of the inside of the printed layer from the top view (Zone 2 in (c)). (For interpretation of the references to color in this figure legend, the reader is referred to the Web version of this article.)

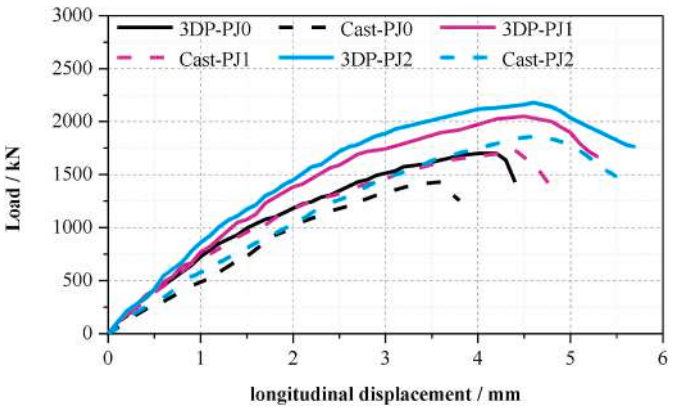

Fig. 20. Axial load-displacement curves of all the tested concrete column specimens.

reinforcement were in elastic state without obvious phenomenon at the initial stage of loading. When the load increased to about 70% of the ultimate load, the steel bars in the column were bent and bulged out, and the transverse cracks appear in the middle of the column, When the load increases to about 70% of the ultimate load, the steel bars in the column are bent and bulged out, and the transverse cracks appeared in the middle of the column. Due to the development of cracks, the concrete of the column body appeared the phenomenon of breaking and peeling off without any sign, and a wide main crack was formed by the combination of several transverse and longitudinal cracks near the loading surface and the inclined cracks of the column body (see Fig. 18(g) and (k)). After the column reached the ultimate load, the value of the press decreased, and the displacement and strain continued to increase. the concrete of the column body continued to peel off, and the specimen failed with concrete crushing (see Fig. 18(h) and (l)). Due to the effect of internal reinforcement, the failure of column has certain ductility.

Fig. 19 shows the permanent formwork of the composite column. As shown in Fig. 19(a), the printed permanent formwork contained a certain amount of PE fibers that provided stress bridging action to a certain extent. As no coarse aggregate was used in the printed permanent formwork, when the composite column was damaged, only a wide main crack appeared and there was no sudden collapse and large area peeling of the column surface. When the permanent formwork was knocked open, it can be seen that the connection between the cast-in-place concrete and the outer permanent formwork had a concave-convex shape, as shown in Fig. 19(b). The coarser inner surface provided better interface adhesion and more reasonable load transfer mechanism between the cast-in-place concrete and the printed permanent formwork, which improved the bearing capacity of the specimen. Additionally, X-ray computed tomography (CT) scanning was conducted by means of a YXLON X-ray micro CT device to investigate the air void content in the printed concrete permanent formwork, especially in the interfaces between the printed layers. Specimens measuring 25 mm × 25 mm × 35 mm, containing three interfaces, were sawn from the printed formwork. An acceleration voltage of 195 kV and beam current of 0.25 mA were applied. The RAW files obtained from the CT device were imported into Matlab 2018b (The Mathworks, US) and processed with a custom script to measure the 2D air void content, given in Fig. 19 (c). Interestingly, a noticeable difference was found in the air void content between the interlayers (i.e. the interfaces between the printed layers) and the printed layers. The interfaces between the layers had the lowest air void content in the specimen (e.g. see Zone 1 in Fig. 19(c) with the air void content of 4.72%). However, the regions inside the printed layers had the highest air void content in the specimen (e.g. see Zone 2 in Fig. 19(c) with the air void content of 11.85%). In addition, comparison between Fig. 19(d) and (e) showed that larger air voids were present at the interfaces between the layers as compared to the inside of the

printed layers, which may be due to the air introduction by the 3DCP process. In general, the mean value of the air void content of the specimens was relatively low (8.35%), contributing to the integrity of the printed concrete permanent formwork.

Fig. 20 shows the axial load-displacement curves of all the tested columns. The reinforcement ratios of the 3DP-PJ0, Cast-PJ0, 3DP-PJ1, Cast-PJ1, 3DP-PJ2 and Cast-PJ2 specimens were 0.0%, 0.0%, 1.9%, 1.9%, 2.5% and 2.5%, respectively. It can be seen in this figure that with the increase of the longitudinal reinforcement ratio, the initial stiffness, as well as the maximum bearing capacity and the corresponding longitudinal displacement of the tested columns increased. This is because the increase of the reinforcement ratio made the column to adjust the stress distribution of the whole section during the loading process, thereby plasticity of the concrete material was well utilized and improved the brittleness of plain concrete under compression.

Compared with the cast-in-place columns with the same reinforcement ratios, the bearing capacity and stiffness of the composite columns made by using the printed concrete as the permanent formwork was improved, which was caused by a higher confinement effect from the printed permanent formwork, and the fact that the strength of the printed concrete for the permanent formwork was 40 MPa, which was higher than that of the cast-in-place concrete (30 MPa). Hence, the results show that under the same conditions, the composite column can obtain a higher bearing capacity and stiffness than the cast-in-place column, simply by a slight increase in the compressive strength of the printed concrete as compared to the cast-in-place concrete. At the same time, it shows that the construction form of the composite column has certain practicability.

4. Conclusions

The 3D concrete printing of permanent formwork for concrete column construction was investigated in this study. Effects of using different HMPC contents and W/B ratios on the printability and mechanical performances of various mixtures were evaluated to identify an optimum mixture. The permanent formworks were 3D printed using the optimum concrete mixture. Conventional steel reinforcement cages, with different longitudinal reinforcement ratios, were then placed inside the printed permanent formworks. The conventional concrete was then poured inside the permanent formworks to construct the composite column specimens. The performances of the composite columns with three different longitudinal reinforcement ratios under pure compression were investigated and the results were compared with those of the counterpart cast-in-place concrete column specimens. The following conclusions can be drawn from this study:

(1) No peeling failure was observed at the printing interval of the 3D printed permanent formwork. The stress at the printing interval was not different from other parts of the printed permanent formwork, confirming its good integrity.
(2) With the same reinforcement ratio, the bearing capacity and stiffness of the composite column (made by using the 3D printed concrete as the permanent formwork) was higher than the counterpart cast-in-place column. This was because of higher confinement effect from the printed concrete permanent formwork, and the higher strength of the printed concrete for making the permanent formwork (40 MPa) than the cast-in-place concrete (30 MPa).
(3) The increase in the longitudinal reinforcement ratio resulted in the increase in the initial stiffness, the maximum bearing capacity and the corresponding longitudinal displacement of both composite columns and cast-in-place columns. Regardless of the reinforcement ratio, the failure of the reinforced concrete columns was due to buckling of the longitudinal reinforcements.
(4) The interface between the cast-in-place concrete and the printed concrete permanent formwork had a concave-convex shape, providing better interface adhesion and load transfer mechanism between the cast-in-place concrete and the printed concrete permanent formwork, and thereby improved the bearing capacity of the composite columns.
(5) The X-ray computed tomography scanning results showed the interfaces between the printed layers of the permanent formwork had the lowest air void content (4.72%) as compared to the regions inside the printed layers (11.85%). However, larger air voids were found at the interfaces between the layers as compared to regions inside the printed layers.

Declaration of competing interest

The authors declare that they have no known competing financial interests or personal relationships that could have appeared to influence the work reported in this paper.

Acknowledgements

This study was funded by the National Key R&D Program of China (2017YFC0703700), Victoria-Jiangsu Innovation and Technology R&D Fund (BZ2020019) and National Natural Science Foundation of China (No. 51778131). The authors would like to thank the Jiangsu Southeast University Testing and Inspection Technology Co. Ltd and School of Materials Science and Engineering, Southeast University for providing instruments and equipment.

References

[1] G.D. Schutter, K. Lesage, V. Mechtcherine, V.N. Nerella, G. Habert, I. Agustí-Juan, Vision of 3D printing with concrete - technical, economic and environmental potentials, Cem. Concr. Res. 112 (2018) 25–36.
[2] B. Nematollahi, M. Xia, J. Sanjayan, Current progress of 3D concrete printing technologies, in: International Symposium on Automation and Robotics in Construction (ISARC), 2017, pp. 260–267.
[3] E. Lloret, A.R. Shahab, M. Linus, R.J. Flatt, F. Gramazio, M. Kohler, S. Langenberg, Complex concrete constructions - merging existing casting techniques with digital fabrication, Comput. Aided Des. 60 (2015) 40–49.
[4] J. Sanjayan, B. Nematollahi, 3D Concrete Printing for Construction Applications, 3D Concrete Printing Technology, Elsevier, 2019, pp. 1–11.
[5] G.W. Ma, Z.J. Li, L. Wang, G. Bai, Micro-cable reinforced geopolymer composite for extrusion-based 3D printing, Mater. Lett. 235 (2019) 144–147.
[6] F.P. Bos, Z.Y. Ahmed, E.R. Jutinov, T.A.M. Salet, Experimental exploration of metal cable as reinforcement in 3D printed concrete, Materials 10 (11) (2017) 1314.
[7] B.R. Zhu, J.L. Pan, B. Nematollahi, Z.X. Zhou, Y. Zhang, J. Sanjayan, Development of 3D printable engineered cementitious composites with ultra-high tensile ductility for digital construction, Mater. Des. (2019), 108088.
[8] M. Hambach, D. Volkmer, Properties of 3D-printed fiber-reinforced Portland cement paste, Cement Concr. Compos. 79 (2017) 62–70.
[9] S-H. Bong, B. Nematollahi, M. Xia, A. Nazari, J. Sanjayan, J.L. Pan, Properties of 3D-Printable Ductile Fiber-Reinforced Geopolymer Composite for Digital Construction Applications, Rheology and Processing of Construction Materials (RheoCon 2019), SCC 2019, Springer, pp. 363-372.
[10] A.R. Arunothayan, B. Nematollahi, R. Ranade, S.-H. Bong, J. Sanjayan, Development of 3D-printable ultra-high performance fiber-reinforced concrete for digital construction, Construct. Build. Mater. 257 (2020), 119546.
[11] B. Nematollahi, P. Vijay, J. Sanjayan, A. Nazari, M. Xia, V.N. Nerella, V. Mechtcherine, Effect of polypropylene fibre addition on properties of geopolymers made by 3D printing for digital construction, Materials 11 (12) (2018) 2352.
[12] G. Vantyghem, W.D. Corte, E. Shakour, O. Amir, 3D printing of a post-tensioned concrete girder designed by topology optimization, Autom. ConStruct. 112 (2020), 103084.
[13] A. Anton, P. Bedarf, A. Yoo, B. Dillenburger, L. Reiter, T. Wangler, R.J. Flatt, Concrete Choreography: Prefabrication of 3D-Printed Columns, Fabricate 2020: Making Resilient Architecture, UCL Press, 2020, pp. 286–293.
[14] T.A.M. Salet, Z.Y. Ahmed, F.P. Bos, H.L.M. Hans, Design of a 3D printed concrete bridge by testing, Virtual, Phys. Prototyp. 13 (3) (2018) 222–236.
[15] J. Kruger, S. Zeranka, Z.G. Van, 3D concrete printing: a lower bound analytical model for buildability performance quantification, Autom. ConStruct. 106 (2019), 102904.
[16] G. Bernardo, A. Telesca, G.L. Valenti, A porosimetric study of calcium sulfoaluminate cement pastes cured at early ages, Cement Concr. Res. 36 (6) (2006) 1042–1047.
[17] Q. Yuan, Z. Li, D. Zhou, T. Huang, A feasible method for measuring the buildability of fresh 3D printing mortar, Construct. Build. Mater. 227 (2019), 116600.

[18] Y. Qian, S. Kawashima, Distinguishing dynamic and static yield stress of fresh cement mortars through thixotropy, Cement Concr. Res. 86 (2018) 288–296.
[19] D. Marchon, S. Kawashima, H. Bessaies-Bey, S. Mantellato, S. Ng, Hydration and rheology control of concrete for digital fabrication: potential admixtures and cement chemistry, Cement Concr. Res. 112 (2018) 96–110.
[20] N.Q. Dzuy, D.V. Boger, Yield stress measurement for concentrated suspensions, J. Rheol. 27 (4) (1983) 321–349.
[21] V.N. Nerella, M.A.B. Beigh, S. Fataei, V. Mechtcherine, Strain-based approach for measuring structural build-up of cement pastes in the context of digital construction, Cement Concr. Res. 115 (2019) 530–544.
[22] R.J.M. Wolfs, F.P. Bos, T.A.M. Salet, Early age mechanical behaviour of 3D printed concrete: numerical modelling and experimental testing, Cement Concr. Res. 106 (2018) 103–116.
[23] T. Voigt, T. Malonn, S.P. Shah, Green and early age compressive strength of extruded cement mortar monitored with compression tests and ultrasonic techniques, Cement Concr. Res. 36 (5) (2006) 858–867.
[24] B. Panda, J.H. Lim, M.J. Tan, Mechanical properties and deformation behaviour of early age concrete in the context of digital construction, Compos. B Eng. 165 (2019) 563–571.
[25] J. Kruger J, S. Zeranka, Z.G. Van, An ab initio approach for thixotropy characterisation of (nanoparticle-infused) 3D printable concrete, Construct. Build. Mater. 224 (2019) 372–386.
[26] Chinese National Standard, Standard for Test Method of Concrete Structures, GB/T 50152, 2012.
[27] L.F. Fan, L.J. Wang, G.W. Ma, P.F. Li, M.J. Xia, et al., Enhanced compressive performance of concrete via 3D-printing reinforcement, J. Zhejiang Univ. - Sci. A. 20 (9) (2019) 675–684.
[28] I. Müller, Influence of Cellulose Ethers on the Kinetics of Early Portland Cement Hydration, Universität Karlsruhe, Karlsruhe, 2006.
[29] D.D. Nguyen, L.P. Devlin, P. Koshy, C.C. Sorrell, Impact of water-soluble cellulose ethers on polymer-modified mortars, J. Mater. Sci. 49 (3) (2014) 923–951.
[30] L.H. Grierson, J.C. Knight, R. Maharaj, The role of calcium ions and lignosulphonate plasticiser in the hydration of cement, Cement Concr. Res. 35 (4) (2005) 631–636.
[31] B. Gyurcsik, L. Nagy, Carbohydrates as ligands: coordination equilibria and structure of the metal complexes, Coord. Chem. Rev. 203 (1) (2000) 81–149.
[32] N. Roussel, H. Bessaies-Bey, S. Kawashima, D. Marchon, K. Vasilic, R. Wolfs, Recent advances on yield stress and elasticity of fresh cement-based materials, Cement Concr. Res. 124 (2019), 105798.
[33] B.G. Ma, Y. Peng, H.B. Tan, S.W. Jian, Z.Z. Zhi, Y.L. Guo, H.H. Qi, T. Zhang, X. Y. He, Effect of hydroxypropyl-methyl cellulose ether on rheology of cement paste plasticized by polycarboxylate superplasticizer, Construct. Build. Mater. 160 (2018) 341–350.
[34] J. Plank, C. Winter, Competitive adsorption between superplasticizer and retarder molecules on mineral binder surface, Cement Concr. Res. 38 (5) (2008) 599–605.
[35] H. Bessaies-Bey, R. Baumann, M. Schmitz, M. Radler, N. Roussel, Organic admixtures and cement particles: competitive adsorption and its macroscopic rheological consequences, Cement Concr. Res. 80 (2016) 1–9.
[36] G. Sang, Y. Zhu, G. Yang, H. Zhang, Preparation and characterization of high porosity cement-based foam material, Construct. Build. Mater. 91 (2015) 133–137.
[37] M. Wyrzykowski, R. Kiesewetter, J. Kaufmann, R. Baumann, P. Lura, Pore structure of mortars with cellulose ether additions–Mercury intrusion porosimetry study, Cement Concr. Compos. 53 (2014) 25–34.
[38] E. Knapen, D.V. Gemert, Cement hydration and microstructure formation in the presence of water-soluble polymers, Cement Concr. Res. 39 (1) (2009) 6–13.
[39] H. Huang, Q. Yuan, D. Deng, J. Peng, Effects of chemical and mineral admixtures on the foam indexes of cement-based materials, Case Stud. Constr. Mater. 11 (2019), e00232.
[40] S.C. Figueiredo, O. Çopuroğlu, E. Schlangen, Effect of viscosity modifier admixture on Portland cement paste hydration and microstructure, Construct. Build. Mater. 212 (2019) 818–840.
[41] N. Roussel, Rheological requirements for printable concretes, Cement Concr. Res. 112 (2018) 76–85.
[42] R.J.M. Wolfs, A.S.J. Suiker, Structural failure during extrusion-based 3D printing processes, Int. J. Adv. Manuf. Technol. 104 (2019) 1–20.